https://doi.org/10.1016/j.combustflame.2020.09.034

Formation of Stabilized Oblique Detonation Waves in a Combustor

Zijian Zhang[a,b], Chihyung Wen[c], Wenshuo Zhang[a,b], Yunfeng Liu[a,b,*], Zonglin Jiang[a,b]

[a] *School of Engineering Science, University of Chinese Academy of Sciences, Beijing 100049, China*

[b] *Institute of Mechanics, Chinese Academy of Sciences, Beijing 100190, China*

[c] *Department of Mechanical Engineering, The Hong Kong Polytechnic University, Kowloon, Hong Kong*

[*] Corresponding author. Fax: +86 10 82543996. *E-mail address:* liuyunfeng@imech.ac.cn (Y. Liu).

Abstract

Initiation and stabilization of oblique detonation waves (ODWs) are important to the successful application of oblique detonation engines (ODEs), which, however, have been rarely studied under realistic combustor conditions. In this study, the flow structures, stabilization characteristics and potential thrust performance (under different combustor's geometries with different ODW reflection locations) in a typical hydrogen-fueled ODE combustor are numerically studied by solving the two-dimensional multi-species Reynolds-averaged conservation equations with a detailed hydrogen combustion mechanism. Results suggest that all the detonation waves/shock waves can be stabilized in the space-confined combustor, and the boundary layer separation induced by the ODW-boundary layer interaction is found crucial to determining the types of combustion mode in the combustor. Except for the expected ODW-induced combustion, fast combustion induced by a stabilized overdriven normal detonation wave (NDW) may exist in the combustor simultaneously (even up to a large extent, >73.7%). It is demonstrated that the stabilization of the overdriven NDW in the combustor can be attributed to the formation of an effective aerodynamic

convergent-divergent nozzle that quickly accelerates the subsonic flow behind the NDW to supersonic, preventing downstream disturbances from propagating upstream. Benefiting from the chemical equilibrium shift caused by the expansion effect of the flow, more heat is released to compensate for the compression loss and the simulated thrust performance is shown not deteriorate significantly even with a large percentage of NDW-induced combustion existing in the ODE combustor. This work would be beneficial to the future developments of the ODEs.

Keywords: oblique detonation wave; combustor; oblique detonation engine; normal detonation wave; boundary layer separation

1. Introduction

Detonative combustion is a supersonic combustion mode with high thermal cycle efficiency, which is implemented through a thin detonation front [1,2]. As a special detonation phenomenon, an oblique detonation wave (ODW) is induced by a supersonic fuel/air combustible mixture flowing through a wedge and is stabilized over the wedge [3-5]. Applying the ODW in a propulsion system, the oblique detonation engine (ODE) is expected to have a simpler geometry, a shorter combustor, and better thrust performance than traditional scramjet engines, and may provide a feasible alternative for hypersonic flight. The ODE has therefore attracted increasing attention in the development of hypersonic air-breathing aircraft [6-8]. Regardless of the possible advantages of this new engine concept, however, a comprehensive understanding of the initiation and subsequent stabilization of a steady ODW in a high-speed flow, especially under combustor operating conditions, will be essential before the ODE can become a reliably workable engine.

Since the concept of ODE was first proposed by Roy in 1946 [9], there have been many experiments

on and simulations of the initiation and stabilization characteristics of ODWs. The stabilization characteristics of ODWs over hypervelocity projectiles launched into premixed combustible gases have been experimentally demonstrated by Kasahara et al. [10,11], Higgins et al. [12] and Verreault et al. [13]. The detailed ODW initiation structure has been found, by Viguier et al. [14] in a two-layer oblique shock tube facility and by Morris et al. [15] in an expansion tube facility, to be composed of a non-reactive oblique shock wave (OSW), a transverse shock wave, and an ODW, intersecting to form a triple point. This is referred to as the abrupted shock-detonation transition structure of the ODW. Another type of ODW initiation structure, namely the smooth transition from a curved OSW to ODW, was numerically observed by Figueira et al. [16] and Papalexandris [17]. At low inflow Mach number, more complex wave structures were also numerically found within the induction zone of ODW, including the internal Chapman-Jouguet (CJ) detonation wave [18] and the secondary detonation wave [19]. Moreover, Choi et al. [20], Higgins et al. [21] and Zhang et al. [22] investigated the instability of oblique detonation surfaces and the corresponding oblique cellular detonation structures via numerical simulations. The effects of inflow Mach number and activation energy on the existence of left-running and right-running transverse waves were identified.

For practical applications, Ren et al. [23,24] numerically investigated wedge-induced ODWs with liquid hydrocarbon fuels and discussed the effects of multiphase characteristics on the stabilization of ODWs. Liu et al. [25], Choi et al. [26] and Fang et al. [27] discussed the effects of expansion waves on the formation of ODW through numerical simulations of the finite wedge-induced ODWs. The quenching phenomenon of ODW may be induced by the interaction of expansion waves with the induction zone. Otherwise, if the finite wedge is long enough, an overdriven ODW would be formed and then interact with the expansion waves emanating from the expansion corner, forming a near-CJ ODW finally. This near-CJ ODW was also found in simulations of the double wedge-induced ODW by Bhattrai et al. [28]. Numerical simulations were also

performed to investigate the effects of inflow equivalence ratio inhomogeneity on the formation of wedge-stabilized ODW by Iwata et al. [29] and Fang et al. [30]. The typical "V-shaped" distorted flame front on the oblique detonation surface was revealed. Moreover, the effects of unsteady inflow with a continuous density/temperature disturbance on wedge-induced ODWs were numerically investigated by Yang et al. [31]. It was found that oscillatory movement of the detonation front is induced but the ability to generate triple points over the detonation front is weakened by this continuous disturbance. Cai et al. [32-34] numerically initiated detonation in supersonic combustible mixtures within a straight channel and a cavity-based channel using a hot jet, and discussed the effects of the contractive passway generated by the hot jet on detonation propagation and further detonation control.

Experimental investigations of ODW and ODE remain challenging, and the reported experimental results are rather limited [35-37]. Previous experimental studies have used only a single wedge or cone to induce ODWs in an unconfined space. In numerical simulations, most results have focused on the initiation, structures, and instability of inviscid ODWs in a semi-infinite space. Few studies have addressed the initiation and stabilization of ODWs under realistic combustor conditions, which are viscous and space-confined, and involve such phenomena as shock/detonation reflection and boundary layer separation [38,39]. Upstream-propagating normal detonation waves (NDWs) are easily formed when ODWs reflect off the combustor walls [40,41], driving the ODE combustor into oscillating mode or even unstart mode. Detonation waves are strong shocks and can induce intense shock-boundary layer interaction in a confined channel, leading to severe boundary layer separation and choking [42], and resulting in unstart of the combustor [43-46]. Therefore, it is imperative to investigate the initiation and stabilization of ODW under realistic ODE combustor conditions, and to take all unstable factors into account, including shock/detonation reflection and boundary layer separation. Notably, under the influence of multiple interactions, complex wave

structures could be formed in the ODE combustor, and the specific combustion mode would not be limited to the expected ODW-induced combustion only. Other combustion modes may occur, resulting in the co-existence of multiple combustion modes. Moreover, it is also necessary to look inside the stable wave structures and the specific combustion modes within the ODE combustor and its corresponding potential thrust performance.

In this study, the two-dimensional (2D) flow fields of a typical ODE combustor fueled by gaseous hydrogen (H_2) are numerically solved using the time-accurate multi-species Reynolds-averaged conservation equations with a detailed chemical mechanism. Following the introduction of the geometry of the ODE combustor in Section 2 and the numerical details in Section 3, the detailed flow structures, stabilization characteristics, and the corresponding combustion modes in the combustor are discussed in Section 4.1. The mechanisms of formation and stabilization of the overdriven NDW are discussed in Section 4.2, and the thrust performance of this combustor in the presence of overdriven NDW are analyzed in Section 4.3. Finally, conclusions are presented in Section 5.

2. Geometry of ODE and its combustor

To theoretically stabilize an ODW over a wedge, the inflow speed must exceed the CJ detonation speed and satisfy the ODW attachment conditions [47], which imposes the requirement of a flight Mach number exceeding 7 for a H_2-fueled ODE. The structure of a typical 2D ODE is composed of three parts: inlet, combustor and nozzle, as schematically shown in Fig. 1a. The high-speed airflow enters the ODE and is compressed by OSWs formed in the inlet. The compressed air is mixed with pre-injected fuel and generates a premixed high-speed combustible mixture. The mixture flows into the combustor, and is first ignited by the strong OSW reflected from the cowl tip and then quickly burned, forming an ODW. The high-speed burnt

products rush through the combustor, expand in the nozzle and then exit the engine, generating thrust. The combustor of the ODE is much shorter than that of a scramjet engine and no isolator is needed, but sufficient length is still required for ODW initiation. Generally, the ODW reflects at least once off the combustor walls. The effects of shock/detonation reflection and subsequent shock/detonation-boundary layer interaction on the stabilization characteristics of the space-confined ODWs in the ODE combustor are the main focus of this study.

The detailed structure of the 2D ODE combustor is presented in Fig. 1b. The combustor is encompassed within points OCDE, where OE is the body wall and CD is the cowl wall. Point O is denoted as the entrance of the combustor and point C is the leading edge of the cowl. AB represents an inlet wall with an incline angle of 25°, while EF represents the nozzle wall with an expansion angle of 20°. The combustor has a length of L = 20 cm (body wall OE) and a height of H = 6 cm. In order to suppress upstream movement of the boundary layer separation zone from the combustor into the inlet [48,49], a simple floor bleed structure, similar to that used in HyShot II [50-52], is located at the entrance of the combustor. The boundary layer established in the inlet is spilled out by the floor bleed structure and the boundary layer is re-established from the combustor entrance.

Ideally, the ODW, formed over the cowl, is expected to reflect at the entrance of the combustor (point O), as shown by the red dash lines in Fig. 1b. In that case, the leading edge of the cowl is located upstream of the combustor's entrance at a distance d, that is C′K = d. Note that d is determined by inflow conditions. However, in practice, due to disturbances generated in the freestream/inlet or the unsteady and inhomogeneous mixing of the fuel, the high-speed air/fuel mixture flowing into the combustor is always unsteady [53,54]. Since the oblique detonation angle is rather sensitive to inflow parameters, an oscillating ODW can easily occur at the combustor's entrance [31], and may reflect at the inlet wall, generating upstream

propagating NDW, and even leading to combustor unstart [40,41]. Therefore, the design leading edge of the cowl (point C) is always placed downstream of its ideal (point C′). Assuming that no flow separation occurs, the corresponding reflection location of the ODW on the body wall (point R) will be downstream of the combustor's entrance (point O), leaving enough space for ODW oscillation, as shown by the red solid lines in Fig. 1b. This design is intended for practical ODE operation at a wide range of flight Mach numbers.

Obviously, the design distance of the cowl's leading edge from its ideal location, C′C, depends on the height of the combustor. Thus, to present results in a more general way, a non-dimensional parameter ξ is introduced in this study to describe the geometry of the ODE combustor:

$$\xi = \frac{\mathrm{C'C}}{H} = \frac{\mathrm{OR}}{H}. \tag{1}$$

$\xi = 0$ means that the ODW reflects at the combustor's entrance, while $\xi > 0$ means that the ODW reflects downstream of the combustor's entrance. In this study, numerical simulations are carried out with several different ξ, to explore the wave structures and their stabilization characteristics in this space-confined ODE combustor.

3. Numerical details

3.1 Physical and mathematical models

The reactive compressible flow field in the ODE combustor is governed by the 2D time-accurate Reynolds-averaged conservation equations of mass, momentum, energy, and species concentration, closed by the Shear-Stress Transport (SST) k-ω turbulence model [55],

$$\frac{\partial \mathbf{U}}{\partial t} + \frac{\partial \left(\mathbf{F} - \mathbf{F}_v\right)}{\partial x} + \frac{\partial \left(\mathbf{G} - \mathbf{G}_v\right)}{\partial y} = \mathbf{S}, \tag{2}$$

where $\mathbf{U}$, $\mathbf{F}$, $\mathbf{G}$, $\mathbf{F}_v$, $\mathbf{G}_v$ and $\mathbf{S}$ are vectors of conservative variables, convective fluxes in the x- and y-directions, diffusive fluxes in the x- and y-directions, and source terms, respectively, and can be expressed as follows,

$$\mathbf{U} = \left[\rho,\, \rho u,\, \rho v,\, \rho e,\, \rho k,\, \rho\omega,\, \rho f_1, \cdots,\, \rho f_{ns-1}\right]^{\mathrm{T}}, \tag{3}$$

$$\mathbf{F} = \left[\rho u,\, \rho u^2 + p,\, \rho uv,\, (\rho e + p)u,\, \rho uk,\, \rho u\omega,\, \rho u f_1, \cdots,\, \rho u f_{ns-1}\right]^{\mathrm{T}}, \tag{4}$$

$$\mathbf{G} = \left[\rho v,\, \rho uv,\, \rho v^2 + p,\, (\rho e + p)v,\, \rho vk,\, \rho v\omega,\, \rho v f_1, \cdots,\, \rho v f_{ns-1}\right]^{\mathrm{T}}, \tag{5}$$

$$\mathbf{F}_v = \left[0,\, \tau_{xx},\, \tau_{xy},\, u\tau_{xx} + v\tau_{xy} + q_x,\, \left(\mu_l + \frac{\mu_t}{\sigma_k}\right)\frac{\partial k}{\partial x},\, \left(\mu_l + \frac{\mu_t}{\sigma_\omega}\right)\frac{\partial \omega}{\partial x},\, \rho D_1 \frac{\partial f_1}{\partial x}, \cdots,\, \rho D_{ns-1}\frac{\partial f_{ns-1}}{\partial x}\right]^{\mathrm{T}}, \tag{6}$$

$$\mathbf{G}_v = \left[0,\, \tau_{yx},\, \tau_{yy},\, u\tau_{yx} + v\tau_{yy} + q_y,\, \left(\mu_l + \frac{\mu_t}{\sigma_k}\right)\frac{\partial k}{\partial y},\, \left(\mu_l + \frac{\mu_t}{\sigma_\omega}\right)\frac{\partial \omega}{\partial y},\, \rho D_1 \frac{\partial f_1}{\partial y}, \cdots,\, \rho D_{ns-1}\frac{\partial f_{ns-1}}{\partial y}\right]^{\mathrm{T}}, \tag{7}$$

$$S = \left[0,\, 0,\, 0,\, 0,\, S_k,\, S_\omega,\, \dot{w}_1, \cdots,\, \dot{w}_{ns-1}\right]^{\mathrm{T}}. \tag{8}$$

Here, ρ, u, v, p, k and ω are the mean density, velocities in the x- and y-directions, pressure, turbulence kinetic energy and turbulence inverse time-scale of the gas mixture, respectively. f_i (i = 1, …, ns) is the mass fraction of the ith species and ns is the total number of species in the gas mixture. The total specific energy e is calculated as

$$e = h - \frac{p}{\rho} + \frac{1}{2}\left(u^2 + v^2\right) + k, \tag{9}$$

where h is the specific enthalpy of the gas mixture, calculated by

$$h = \sum_{i=1}^{ns} f_i h_i, \tag{10}$$

with the specific enthalpy of each species, h_i, obtained from the piecewise fourth-order temperature polynomial fitting of NASA [56]. Assuming each species as a perfect gas, the equation of state of the gas mixture is given by

$$p = \sum_{i=1}^{ns} \rho f_i \frac{R_0}{W_i} T, \tag{11}$$

where T is the temperature of the gas mixture, R_0 (= 8.314 J/(mol·K)) the universal gas constant, and W_i the molecular weight of species i.

In Eqs. (6) and (7), the components of the viscous stress tensor are calculated by

$$\begin{cases} \tau_{xx} = \left(\mu_l + \mu_t\right)\cdot\left(\dfrac{4}{3}\dfrac{\partial u}{\partial x} - \dfrac{2}{3}\dfrac{\partial v}{\partial y}\right) - \dfrac{2}{3}\rho k \\ \tau_{yy} = \left(\mu_l + \mu_t\right)\cdot\left(\dfrac{4}{3}\dfrac{\partial v}{\partial y} - \dfrac{2}{3}\dfrac{\partial u}{\partial x}\right) - \dfrac{2}{3}\rho k \\ \tau_{xy} = \tau_{yx} = \left(\mu_l + \mu_t\right)\cdot\left(\dfrac{\partial v}{\partial x} + \dfrac{\partial u}{\partial y}\right) \end{cases}, \tag{12}$$

where μ_l is the laminar dynamic viscosity of the gas mixture evaluated by Wilke's mixing rule [57], while μ_t is the turbulence dynamic viscosity. The μ_t, the model constants σ_k and σ_ω in Eqs. (6) and (7) and the turbulence source terms S_k and S_ω in Eq. (8), are evaluated by the SST k-ω turbulence model. The heat flux is assumed to obey Fourier's law with inter-species diffusions taken into account, and its components can be expressed as

$$\begin{cases} q_x = -\left(\kappa_l + \kappa_t\right)\cdot\dfrac{\partial T}{\partial x} - \sum_{i=1}^{ns}\rho D_i h_i \dfrac{\partial f_i}{\partial x} \\ q_y = -\left(\kappa_l + \kappa_t\right)\cdot\dfrac{\partial T}{\partial y} - \sum_{i=1}^{ns}\rho D_i h_i \dfrac{\partial f_i}{\partial y} \end{cases}, \tag{13}$$

where κ_l is the laminar thermal conductivity of the gas mixture evaluated by Wilke's mixing rule [57], and κ_t is the turbulence thermal conductivity calculated via the turbulence Prandtl number Pr_t.

$$\kappa_t = \frac{c_p \mu_t}{\mathrm{Pr}_t}, \quad \text{with } \mathrm{Pr}_t = 0.9, \tag{14}$$

where c_p is the specific heat at constant pressure. In Eqs. (6), (7), and (13), D_i is the species mass diffusion coefficient and can be evaluated by a multi-component diffusion model with thermal and pressure diffusions.

Additionally, the species mass production rate $\dot{w}_i$ in Eq. (8) is modelled by the Jachimowski H_2 combustion mechanism [58], which involves 19 reversible elementary reactions among 9 species: H_2, H, O_2, O, OH, HO_2, H_2O_2, H_2O and N_2. This detailed chemistry mechanism has been shown to be capable of providing good predictions of the laminar flame speed, adiabatic flame temperature, and ignition delay when compared with experiments [59]. It has also been successfully applied to shock-induced combustion [60]

and detonation [26] simulations. In Figs. S1 and S2 of the Supplementary Materials, the pressure, temperature, and H_2 distributions in the ODE combustor of $\xi = 1$ simulated using this combustion mechanism is compared with those using an updated H_2 combustion mechanism of Burke et al. [61] for high-pressure combustion. Results show that these two combustion mechanisms reveal almost the same flow field and flow parameter distributions for the present combustor and the differences are negligible.

Further, the temperature behind the detonation wave is always above 3000 K, where the vibrational excitation of O_2, H_2O, HO_2, etc. become noticeable in this temperature range. Since the piecewise fourth-order temperature polynomial of NASA [56] is used to fit the properties of each species, thermal equilibrium is automatically considered in this study. In the recent studies [62-65], thermal nonequilibrium effect has been shown to have non-negligible influences on the predictions of detonation induction length and consequently detonation cell size. However, by comparison of the simulated thermal equilibrium case and the thermal nonequilibrium case using the Park's two-temperature kinetic model [66], the flow field in the ODE combustor in this study is shown not sensitive to the detailed detonation structure, as illustrated in Figs. S3 and S4 of the Supplementary Materials. Therefore, the thermal nonequilibrium effect and the corresponding vibrational excitation-chemistry coupling are not considered in the present simulation for simplicity. The vibrational nonequilibrium effects on the detailed flow structures, stabilization characteristics, and the corresponding combustion modes in the combustor will be further investigated detailedly in the future. On the other hand, since the flow entering the ODE combustor is premixed and combustion is then induced by shock waves and completed quickly through thin detonation fronts, the turbulence-chemistry interaction is expected to have a rather small effect on the combustion rate for this type of premixed detonation flame. Therefore, the turbulence-chemistry interaction is not considered as well in this study.

3.2 Numerical algorithm

The above governing equations are numerically solved by a quadrilateral-grid-based finite volume method [67]. The equations are discretized spatially by a second-order upwind total variation diminishing (TVD) scheme with a new multi-dimensional polynomial interpolation framework. The non-linear Harten-Lax-van Leer contact (HLLC) approximate Riemann solver [68] is used to define interface fluxes with entropy and positivity conditions automatically satisfied. The minmod limiter is employed to suppress spurious oscillations near the discontinuities, and still preserve high-order accuracy away from the discontinuities. In the time dimension, the equations are implicitly integrated by a dual time-stepping method in combination with an operator-splitting method [69]. The operator-splitting method is employed to treat chemical source terms and to overcome the stiffness problems caused by the mismatch of time scales between chemical reactions and flows.

Because the flow field in the ODE combustor mainly involves boundary layer separations, shock waves and shock-induced combustion, two relevant classical cases, namely the hypersonic shock wave-turbulent boundary layer interaction experiment conducted by Schülein [70] and the unsteady shock-induced combustion experiment over a hypervelocity projectile conducted by Lehr [71], are tested and compared with the experimental data to validate the capabilities of the above-mentioned numerical algorithm in ODE combustor simulations. As shown in the Supplementary Materials (Figs. S5-S8), the above numerical algorithm is proven to be capable of capturing the hypersonic boundary layer separation phenomenon and the features of shock-induced combustion.

Table 1 Geometrical parameters of 5 different ODE combustors and their corresponding grid cell numbers (with the same length, L, of 20 cm and height, H, of 6 cm).

Case No.	Length of CK	Value of ξ	Total grid cells
1	11 cm	0	2.59 million
2	9 cm	1/3	2.35 million
3	7 cm	2/3	2.23 million
4	5 cm	1	2.00 million
5	3 cm	4/3	1.89 million

3.3 Cases

The ODE is expected to be operated at an altitude of 30 km with a flight Mach number of $Ma_f = 9$. For reliable ODE operation, as explained in Section 2, it is always preferable for the reflection of the ODW at the body wall to occur downstream of the combustor's entrance. The subsequent effects of shock/detonation-boundary layer interaction should be considered to evaluate the performance of the ODE combustor. Therefore, five different geometries of the 6-cm high ODE combustor characterized by different ξ values are studied in this paper, as summarized in Table 1.

Since the flow field and the corresponding stabilization characteristics of the space-confined ODWs in the ODE combustor are the focus of this study, the complex processes of fuel (H_2) injection and subsequent mixing with air in the ODE inlet are not considered here. Following Refs. [30] and [72], the freestream is assumed to be pre-compressed twice by two weak OSWs generated by the two 12.5°-ramps in the inlet before it enters the ODE combustor (see Fig. 1a), and the injection of H_2 and its subsequent mixing with air are assumed to be completed downstream of these two OSWs. Further, we assume ideally that the flow parameters (pressure, temperature and velocity) in the inlet are not influenced by the injection and mixing processes. Consequently, a uniform premixed H_2/air inflow, parallel to the end of the inlet (25° to the *x*-

direction), is assumed to enter the combustor, and this serves as the inflow condition of the simulations in this study, as shown in Fig. 1b. For a flight Mach number of Ma_f = 9 at an altitude of 30 km, the static pressure, temperature, and velocity of the stoichiometric H_2/air inflow are p_i = 43.96 kPa, T_i = 855.1 K and V_i = 2466 m/s, respectively. The corresponding inflow Mach number and d (the ideal distance of the leading edge of the cowl upstream of the combustor's entrance, Fig. 1b) are Ma_i = 3.629 and d = 11 cm, respectively. As for other boundary conditions, the no-slip iso-thermal (T_w = 300 K) condition is set at all wall boundaries, and the supersonic outflow condition is set at all outflow boundaries.

Quadrilateral grid cells are used in this study. The maximum grid size is limited to 0.1 mm in the main combustion zone and the grids are clustered near walls with a minimum grid height of 0.002 mm (y+ = 0.74), resulting in a total of 1.89~2.59 million grid cells for the ODE combustors with different ξ values (Table 1). Resolution studies were carefully carried out to confirm the grid independence of the simulated flow fields (See Section 4.1).

4. Results and discussions

4.1 Flow structure study and grid independence test

For the ξ = 0 case where the ODW reflects at the combustor's entrance, the time-accurate simulation results suggest that the shock waves/detonation waves stabilize in the space-confined ODE combustor and the flow field achieves steady state. The final steady flow field in the combustor is exhibited in the numerical shadowgraph and H_2 mass fraction contours in Fig. 2. An OSW is first formed over the cowl when the supersonic premixed combustible mixture flows into the combustor. After a short induction zone, the OSW transits into an ODW without obvious transverse waves and consequently the classical smooth OSW-ODW transition pattern is formed. As the flow crosses the ODW, the mass fraction of H_2 drops abruptly to a rather

low level, implying that fast combustion is induced by the ODW. Therefore, only a short combustor is needed in this kind of hypersonic air-breathing engines, which is one of the major advantages of ODEs. When the ODW reflects at the combustor's entrance (at the body wall), a reflected shock wave (RfSW) is formed and then reflects repeatedly between the cowl wall and the body wall in the combustor. In the process of multiple reflections, the strength of the RfSW weakens downstream, eventually meeting the expansion fan at the outlet of the combustor.

The distributions of flow parameters along the centerline of the combustion chamber (y = 3 cm) are plotted in Fig. 3. As the flow crosses the ODW, the H_2 mass fraction drops abruptly from its original value of 0.0285 to about 0.005, while the temperature increases from 855.1 K to about 3000 K, demonstrating two standard features of a detonation wave. Moreover, the maximum pressure ratio across the ODW is about 9.87. All these values agree well with the theoretical solutions of a flow across an ODW over a 25° wedge angle: $H_{2,CJ}$ = 0.00522, T_{CJ} = 3086 K and p_{von}/p_i = 10.17, where the subscript CJ represents the CJ condition, and p_{von} and p_i are the von Neumann pressure and the initial pressure, respectively. The combustion mode of ODW is confirmed again by these changes of flow parameters. Notably, the multiple pressure jumps behind repeated RfSWs are also clearly identified in Fig. 3.

For reflection locations of the ODW at the body wall downstream of the combustor's entrance (that is, $\xi > 0$), time-accurate simulation results also confirm that shock waves/detonation waves remain stable in these space-confined ODE combustors with different geometries, and the flow fields of these cases (Cases 2-5) are all steady. However, compared with Case 1, new flow structures emerge and the final steady flow fields are rather different and fairly complicated, as shown in numerical shadowgraphs in Fig. 4. Isolines of Ma = 1 are also provided to show the demarcation lines between the subsonic and supersonic zones. For ξ = 1/3 in Case 2 (Fig. 4a), the ODW does not reflect at the body wall directly, but forms a classical

OSW/boundary layer separation flow pattern. When the ODW reflects over the separation zone near the body wall, a RfSW forms near the reflection point, and a reattachment shock wave (RaSW) is also formed in the downstream region of the separation zone. The RfSW and RaSW weaken after multiple reflections between the combustor's walls. A separation shock wave (SSW) is formed ahead of the separation zone, and another shock wave, almost normal to the incoming flow, is formed between the incident ODW and the SSW. This normal shock wave (NSW) will be shown to be an overdriven NDW. Behind the NDW, a finite subsonic zone is presented.

The flow fields of Cases 3-5 are quite similar to that of Case 2, with only the sizes of the flow structures being different. As ξ increases from 1/3 to 4/3 (from Case 2 to Case 5), the lengths of the SSW and NDW become longer and longer, the size of the subsonic zone behind the NDW grows larger and larger, and the length of the ODW becomes shorter and shorter. The size of the separation zone only grows when ξ is small and then remains a similar size for large ξ. Furthermore, as in $\xi \geq 2/3$ (Cases 3-5), an obvious subsonic zone is formed when the RfSW reflects at the cowl wall. This subsonic zone connects with the subsonic zone induced by the NDW for $\xi = 1$ and 4/3 (Cases 4 and 5), and this results in a large subsonic zone spanning the height of the ODE combustor. However, this large subsonic zone would not extend far downstream in the combustor, so the stabilization of the shock waves/detonation waves within the combustor would not be affected.

The flow field of the ODE combustor with $\xi = 1$ (Case 4) serves as an illustrative example for analysis of the detailed combustion modes of the ODE combustors. In this case, the ODW reflection location is designed to be downstream of the combustor entrance. Figure 5 shows the contours of H_2 mass fraction along with pressure isolines in this combustor. The leading shock front is composed of three parts: the ODW, NDW and SSW (the OSW can be thought of as a subpart of the ODW). Fast combustion is induced by the ODW,

NDW and SSW, since H_2 mass fraction drops abruptly to a rather low level across these waves. This feature can also be clearly seen in the distributions of flow parameters at various heights along the combustor's length, as demonstrated in Fig. 6. A pressure ratio of 9.71 can be obtained at y = 5 cm where the flow crosses the ODW (Fig. 6a); this is similar to that in Case 1 (9.87, Fig. 3). The temperature increases to about 3000 K, and the H_2 mass fraction drops to about 0.005. All of these values agree well with the theoretical solutions of flow across an ODW over a 25° wedge angle, as in Case 1. After the ODW, the pressure jump behind the RfSW can be clearly seen in Fig. 6a. In Fig. 6b, the H_2 mass fraction is seen to drop abruptly at the NDW, to about 0.006, from compression at the NDW, and the temperature suddenly increases to about 3000 K. Moreover, the maximum pressure ratio across the NDW is about 14.88, which is very close to the theoretical value of 15.32 for the corresponding overdriven detonation wave. These results together confirm that the normal shock front in this case is really an overdriven detonation wave.

The SSW is a little different. As indicated in Fig. 4c, the deflection angle of the flow across this SSW is about 21°. Figure 6c shows that the temperature behind this SSW can reach about 3000 K, and the H_2 mass fraction drops abruptly to a rather low value of about 0.005; these parameters agree well with the corresponding CJ values across a theoretical 21° ODW: T_{CJ} = 3024 and $H_{2,CJ}$ = 0.00488. However, the pressure ratio across this SSW is about 5.66, which is between the values across a theoretical 21° ODW (9.30) and a 21° OSW (4.71). The present SSW is neither a true OSW nor a true ODW. This may be because this SSW is relatively weak (the deflection angle of flow across this SSW is relatively small) and thus yields a relatively long induction length during OSW-ODW transition. This fairly short SSW has not yet developed into its final ODW form.

To exclude the effects of grid size on the flow field in the ODE combustor, grid independence tests were carefully carried out with different grid sizes. For ξ = 1 (Case 4), two grid sizes were used in the simulations

and the results are compared in Figs. 5 and 6. In the first configuration, the maximum grid size is limited to 0.1 mm in the main combustion zone (where the detonation waves exist) and the grid height clustered at all walls is 0.002 mm ($y+$ = 0.74), resulting in a total of 2.00 million grid cells, as illuminated in Section 3.3. The second grid configuration has twice the grid resolution in both directions. The maximum grid size is limited to 0.05 mm in the main combustion zone and the grid height clustered at all walls is 0.001 mm ($y+$ = 0.37), resulting in a total of 7.06 million grid cells (about 3.5 times that of the first grid configuration). As indicated in Fig. 5, the differences in the contours of H_2 mass fraction and pressure between these two grid resolutions can be neglected. Moreover, the distributions of flow parameters (across different shock/detonation fronts in the combustor) with these two grid resolutions nearly overlap with each other, as shown in Fig. 6. Therefore, the grid resolution with a maximum grid size of 0.1 mm in the main combustion zone and a grid height of 0.002 mm near the walls is considered sufficient to resolve the key flow structures in the ODE combustor in this study.

4.2 Formation and stabilization of overdriven NDW

It is interesting that an overdriven NDW is formed and stabilized within the space-confined ODE combustor. Overdriven NDW is commonly formed over a hypervelocity blunt projectile shot into a premixed combustible gas [10-12], but there is no such a blunt structure supporting the overdriven NDW in the ODE combustor. On the other hand, previous studies [40,41] have indicated that, when an overdriven NDW is formed within a channel (the combustor), it always propagates upstream and will not be stabilized at a specific location. Therefore, to understand the stabilization characteristics of the flow field in the ODE combustor, it is imperative to determine how this overdriven NDW is formed and why this overdriven NDW is stabilized in the ODE combustor.

Taking the geometry of the ODE combustor with $\xi = 1$ (Case 4) as an example, the process of the establishment of the flow field is shown in Fig. 7 by numerical shadowgraphs (a video-clip is attached). As indicated in Fig. 7a, when the ODW has been fully established and reflects at the body wall downstream of the combustor's entrance, it interacts with the boundary layer and begins to form the classical ODW/boundary layer separation flow structures, including a separation zone, a SSW, a RfSW and a RaSW. After that, the size of the separation zone and the length of the SSW increase gradually as the separation point and the SSW move upstream, as shown in Figs. 7b and 7c. The upstream movements of the separation point and the SSW stop at the combustor's entrance, and then the strength of the SSW increases gradually along with the increment of the shock angle of the SSW, as shown in Fig. 7d. At $t = 0.21$ ms (Fig. 7e), a flow pattern of regular reflection between the ODW and SSW is formed, but this regular reflection pattern is not stable and is in fact just an intermediate state of the flow field. Figure 8 shows the shock polar relationships of this reflection pattern. The shock polars of the RfSWs of the ODW and SSW are detached from each other, and there is no physical state (the intersection point of the shock polars of the RfSWs) for the stable existence of such a regular reflection. Therefore, the regular reflection pattern transits to the Mach reflection quickly, and consequently a Mach stem, namely the overdriven NDW, is formed, as shown in Fig. 7f. As the flow process proceeds, the length of the overdriven NDW increases gradually and reaches its stable state after $t =$ 0.8 ms (Fig. 7g). Finally, the stable flow field is formed in the ODE combustor. In sum, it is the mismatch between the RfSW state of the ODW and that of the SSW which forms and supports the overdriven NDW in the ODE combustor, when the ODW interacts with the SSW.

Meanwhile, the size and shape of the separation zone change in an opposite way after the formation of the overdriven NDW. As indicated in Figs. 7e–7h, when the overdriven NDW is first formed, the separation zone has reached its maximum size. After that, the overdriven NDW grows and moves upstream, while the

corresponding triple points also move upstream. The total size of the separation zone decreases as well and finally reaches its stable state.

As indicated in Fig. 7h, due to the differences in flow parameters (density, temperature, velocity) between the flow across the NDW and that across the ODW (or the SSW) and its RfSW, a slip line is formed behind each triple point of the overdriven NDW. The two slip lines form a flow path behind the overdriven NDW, and then the gas compressed by the overdriven NDW passes within this flow path, as depicted in Fig. 9. Two streamlines (Streamlines 1 and 3) are used to indicate the boundaries of the full flow path before and behind the overdriven NDW. It can be seen that the flow path is not a straight stream channel with a constant width, so the flow parameters vary along this flow path. The width of the flow path can be defined as the length of the cross-section (marked as the green lines in Fig. 9) perpendicular to each streamline. Figure 10 shows the variation of the width of this flow path along the combustor, along with the Mach number along Streamline 2 (See Fig. 9). After the compression of the NDW, the flow path first converges and then diverges to form an effective aerodynamic convergent-divergent nozzle (an effective aerodynamic Laval nozzle).

As the flow passes through this effective aerodynamic throat, the subsonic flow behind the overdriven NDW is accelerated to supersonic, forming a finite subsonic zone. Disturbances in the supersonic zone behind this subsonic zone in the combustor will neither propagate to the NDW nor affect its stabilization. Otherwise, as previously indicated in Refs. [40,41], the upstream propagation of the overdriven NDW by Mach reflection in the confined channel is caused by the large subsonic zone behind the NDW, which propagates downstream disturbances upstream. The effective aerodynamic convergent-divergent nozzle formed between the two slip lines behind the ends of the overdriven NDW accelerates the subsonic flow behind the overdriven NDW to supersonic and prevents downstream disturbances from propagating upstream. Consequently, the overdriven NDW in the ODE combustor is stabilized.

Further examining Figs. 8 and 9, it can be found that the formation of the convergent section of this effective aerodynamic convergent-divergent nozzle is related to the relative flow angles behind the NDW near the upper and lower triple points, while the formation of the divergent section is related to the shape of the boundary layer separation zone. In Fig. 8, the flow angle behind the NDW near the upper triple point (near the side of ODW) is about 9.8°, which is significantly smaller than the value of 31.9° near the lower triple point (near the side of SSW), resulting in a convergent flow path behind the NDW. Additionally, except for the flow stabilization effect of this effective aerodynamic convergent-divergent nozzle, it will be shown later in Section 4.3 that this nozzle also has an effect of shifting the chemical equilibrium to release more heat into the flow, which is helpful to compensate for the compression loss of the NDW and consequently yields a robust potential thrust performance of the combustor.

4.3 Thrust potential analysis

As discussed above, combustion in the ODE combustor is enabled by an ODW, a NDW or a SSW, depending on the specific geometry of the combustor. Quantitatively, the percentages of different combustion modes in ODE combustors with different geometries are shown in Fig. 11a. Notably, the percentage of a specific combustion mode (the ODW-induced combustion, the NDW-induced combustion or the SSW-induced combustion) is defined by the percentage of the mass flow rate across the corresponding type of shock front (ODW, NDW or SSW) in the total mass flow rate entering the combustor. Since the inflow is uniform, the percentage of a specific combustion mode can be calculated from the projected length of the corresponding shock front in the direction perpendicular to the inflow. For the geometry of $\xi = 0$, combustion in the combustor is only induced by the ODW, while combustion is induced by the ODW, NDW and SSW at the same time for $\xi > 0$. Further, as ξ increases from 0 to 4/3, the percentage of ODW-induced combustion

decreases from 100% to 12.8%, while the percentage increases from 0 to 13.5% for SSW-induced combustion, and, significantly, from 0 to 73.7% for NDW-induced combustion. As is known, the incoming flow experiences the compression of an OSW before combustion for the ODW, but experiences the compression of a NSW before combustion with the NDW. The total pressure loss of a NSW is much larger than that of an OSW for the same incoming flow, which implies that the thrust reduction due to the NDW is much higher than that due to an ODW. Therefore, it is important to analyze the thrust performance of the ODE combustor given the presence of the NDW, and compare it with that of the ODE combustor with only ODW-induced combustion.

To evaluate the thrust performance of the ODE combustor in a quantitative way, the concept of thrust potential, proposed by Riggins et al. [73,74] and widely used (See Refs. [48,49,75,76]), can be employed to estimate the ideal capability of the flow to do work. As indicated in Fig. 12, for the flow state at an arbitrary Point 2 on an arbitrary plane *a* in the combustor, another ideal flow state at an imaginary Point 3 can be found through an ideal isentropic expansion to the ambient pressure (with frozen chemistry), then the thrust potential at Point 2 can be evaluated by

$$F_{\text{pot}}\Big|_2 = \frac{\rho_3\left(u_3^2+v_3^2\right)+p_3}{\rho_3\sqrt{u_3^2+v_3^2}} - F_{\text{ref}}, \tag{15}$$

where F_{ref} is the thrust potential on the reference plane, which can be arbitrarily set as $F_{\text{ref}} = 0$. The thrust performance of an engine can also be expressed in the form of specific impulse, i.e., thrust per weight of fuel, as follows,

$$I_{\text{pot}}\Big|_2 = \frac{F_{\text{pot}}\Big|_2}{f_{\text{fuel}}g}, \tag{16}$$

where f_{fuel} is the mass fraction of fuel (H_2) in the mixture and g is the acceleration of gravity. Moreover, for the Point 2 in the combustor, a Point 1 can also be found in the plane *i* upstream of the combustor by tracing

upstream along the streamline. Subtracting the thrust potential at Point 1 to exclude the potential work contributed by the compressive incoming flow, ΔI_{pot} can be thought of as the addition of thrust potential by the combustor at Point 2,

$$\Delta I_{\text{pot}}\Big|_{1\to 2} = I_{\text{pot}}\Big|_2 - I_{\text{pot}}\Big|_1 . \tag{17}$$

Clearly in Eq. (17), the choice of F_{ref} would not affect the estimate of ΔI_{pot}. Further, the total thrust potential addition by the combustor at Plane *a* can be evaluated by the following integration,

$$\Delta I_{\text{pot}}\Big|_{i\to a} = \frac{\int_e F_{\text{pot}}\mathrm{d}\dot{m} - \int_i F_{\text{pot}}\mathrm{d}\dot{m}}{f_{\text{fuel}} g \cdot \int \mathrm{d}\dot{m}}, \tag{18}$$

where $\mathrm{d}\dot{m}$ is the mass flow rate of the differential element of the mixture.

Table 2 Theoretical additions of thrust potential by different combustion modes.

Combustion mode	ΔI_{pot} /s^{-1}
NDW	1004.3
25° ODW	1658.4
21° ODW	1774.2

According to the theoretical solutions of the overdriven NDW and ODWs, the theoretical additions of thrust potential by different combustion modes can be obtained; they are summarized in Table 2. The ODW in the present ODE combustor has a 25° deflection angle, but the SSW is an incomplete ODW with a deflection angle of 21°. The theoretical addition of thrust potential by a 21° ODW is used here to analyze the theoretical thrust performance of the SSW for simplicity. As revealed in Table 2, the thrust performance of the NDW is much lower than that of an ODW because of the larger compression loss.

The theoretical total thrust potential additions of the ODE combustors with different geometries can be

estimated from the different combustion modes based on their percentage of the combustor cross-section, as shown in Fig. 11b. As shown, due to the low thrust performance of the NDW and its large percentage at large ξ, the theoretical thrust performance of the ODE combustor decreases obviously with an increase of ξ. The simulated thrust performance of the ODE combustors at the combustor outlet (x = 0.2 m) are shown with the theoretical predictions in Fig. 11b. It indicates that the simulated thrust performance of the ODE combustor with pure ODW-induced combustion (ξ = 0) is slightly lower than the theoretical prediction. Also, although the theoretical thrust performance decreases obviously at large ξ, the simulated thrust performance of the combustor does not change much with ξ. To explain these discrepancies, the distributions of simulated thrust potential addition along the combustor's height at the outlet (x = 0.2 m) are extracted in Fig. 13.

As indicated in Fig. 13, the simulated thrust potential addition for the ξ = 0 case overlaps with the theoretical value for a 25° ODW in most parts of the combustor, except near the cowl and body walls (y = 0 and 0.06 m). The abrupt drops near the cowl and body walls are mainly caused by the low-speed flow in the boundary layer. In the cases with ξ > 0, the distributions of simulated thrust potential addition in the core flow are not uniform. For every ξ > 0 case, the simulated addition of thrust potential generated by the ODW close to the cowl wall (y = 0.06 m) is slightly larger than the theoretical value for a 25° ODW, while the simulated addition by the SSW close to the body wall (y = 0) is much lower than its theoretical counterpart of a 21° ODW. As for the overdriven NDW, the simulated thrust potential addition is much larger than that by a theoretical overdriven NDW.

The distributions of simulated thrust potential additions along the streamlines across the middle parts of different shock fronts are given in Fig. 14, together with the distributions of H_2 mass fraction. It can be revealed that the thrust potential addition and H_2 mass fraction agree with those for a theoretical 25° ODW for ξ = 0 in Case 1 (Fig. 14a). Nevertheless, for the one crossing the ODW in Case 4 (taken as an example

of $\xi > 0$), the thrust potential addition first increases to approach the theoretical value and then increases slightly again later (Fig. 14b). Correspondingly, the H_2 mass fraction for the ODW in Case 4 decreases when it approaches its theoretical value. Reexamination of the stream channel between Streamline 1 and the cowl wall behind the ODW in Fig. 9 suggests that the further increase of the simulated thrust potential addition may be caused by the expansion of the flow behind the ODW, which shifts the chemical equilibrium of combustion toward the direction of producing products and releases more heat into the flow. This can be confirmed by comparing the thrust potential addition and H_2 mass fraction with the theoretical values for the NDW in Fig. 14c. The thrust potential addition behind the NDW first increases to reach the theoretical value and then further increases to a much larger value by expansion within the effective aerodynamic convergent-divergent nozzle, leading to the real H_2 mass fraction decreasing to a much lower value. As for the flow crossing the SSW in Case 4 (Fig. 14d), the loss caused by the RaSW reduces the thrust potential addition significantly after it reaches its theoretical value. To conclude, the chemical equilibrium shift caused by the expansion of the flows behind the ODW and NDW in the combustor compensates for the loss of the overdriven NDW and consequently causes the simulated total addition of thrust potential not to deteriorate significantly, even in the presence of a large percentage of NDW.

5. Conclusions

The ODE is a promising hypersonic air-breathing propulsion engine that is characterized by high thermal cycle efficiency and fast combustion, and is expected to be operated at high Mach number. Before the ODE becomes a reliably workable engine, however, a comprehensive understanding of initiation and subsequent stabilization of a steady ODW within the ODE combustor will be necessary. In this study, the 2D flow fields in a typical ODE combustor are numerically solved using the time-accurate multi-species

Reynolds-averaged conservation equations with the detailed Jachimowski H_2 combustion mechanism. The wave structures and their corresponding stabilization characteristics were analyzed considering various combustor geometries with different ODW reflection locations under the regular reflection assumption (different ξ values). Results suggest that all the detonation waves/shock waves can be stabilized in combustors with different ξ. For the geometry of combustor with the ODW reflecting at the combustor's entrance ($\xi = 0$), the flow field is stable and fast combustion is only induced by a stabilized ODW. In the geometry of the combustor with the ODW reflecting downstream of the combustor's entrance ($\xi > 0$), the classical flow structures of ODW-boundary layer separation appear in the combustor together with an overdriven NDW. The flow field is still stable, even with the existence of the overdriven NDW, and corresponding fast combustion is contributed by the ODW, NDW and SSW simultaneously. As ξ increases from 0 to 4/3, the percentage of ODW-induced combustion decreases from 100% to 12.8%, while the percentage increases from 0 to 13.5% for SSW-induced combustion and from 0 to 73.7% for NDW-induced combustion, respectively.

After the establishment of the flow field in the ODE combustor is described, the formation of the overdriven NDW is analyzed by the shock polar as the result of Mach reflection between the incident ODW and the SSW formed by the boundary layer separation induced by the ODW-boundary layer interaction. The overdriven NDW is stabilized in the combustor by the formation of an effective aerodynamic convergent-divergent nozzle, which accelerates the subsonic flow behind the overdriven NDW to supersonic and prevents downstream disturbances from propagating upstream. Although the existence of the overdriven NDW would theoretically decrease the thrust performance of the ODE combustor due to increased compression loss, the simulated thrust performance does not deteriorate significantly. The chemical equilibrium shift caused by the flow expansion behind the ODW and the NDW in the combustor releases

more heat into the flow and compensates for the loss of the overdriven NDW.

The above numerical simulation results and analyses serve as the guidelines for the future development of the experimental ODE models to validate the wave structures and stabilization characteristics in the combustor. In Fig. S9 of the Supplementary Materials, an experimental Schlieren image of the flow field in an ODE combustor [77] obtained in a hypersonic wind tunnel [78] is presented and compared with the corresponding numerical simulation. This preliminary experimental data clearly validates the wave structures and stabilization characteristics demonstrated in this numerical study.

Acknowledgements

This work was supported by the National Natural Science Foundation of China (Grant Nos. 11672312, 11532014, and 11772284).

Supplementary material

A supplementary document contains the validation cases of numerical methods, the comparison cases of different combustion mechanisms and different thermal equilibrium/nonequilibrium models, and the preliminary experiment result about the formation of stabilized detonation waves in an ODE combustor.

A video-clip, taking $\xi = 1$ as an example, shows the process of the establishment of the flow field in the ODE combustor.

References

[1] E.M. Braun, F.K. Lu, D.R. Wilson, J.A. Camberos, Airbreathing rotating detonation wave engine cycle analysis, Aerosp. Sci. Technol. 27 (2013) 201-208.

[2] F.K. Lu, E.M. Braun, Rotating Detonation Wave Propulsion: Experimental Challenges, Modeling, and Engine Concepts, J. Propuls. Power 30 (5) (2014) 1125-1142.

[3] Y. Zhang, Y. Fang, H.D. Ng, H. Teng, Numerical investigation on the initiation of oblique detonation waves in stoichiometric acetylene–oxygen mixtures with high argon dilution, Combust. Flame 204 (2019) 391-396.

[4] C. Tian, H. Teng, H.D. Ng, Numerical investigation of oblique detonation structure in hydrogen-oxygen mixtures with Ar dilution, Fuel 252 (2019) 496-503.

[5] Y. Fang, Y. Zhang, X. Deng, H. Teng, Structure of wedge-induced oblique detonation in acetylene-oxygen-argon mixtures, Phys. Fluids 31 (2) (2019) 026198.

[6] K. Kailasanath, Recent developments in the research on pulse detonation engines, AIAA J. 41 (2) (2003) 145-159.

[7] A.J. Higgins, Ram accelerators: outstanding issues and new directions, J. Propuls. Power 22 (6) (2006) 1170-1187.

[8] P. Wolański, Detonative propulsion, Proc. Combust. Inst. 34 (1) (2013) 125-158.

[9] M.M. Roy, Moteurs thermiques, Comptes Rendus de l'Académie des Sciences 222 (1) 1946.

[10] J. Kasahara, T. Fujiwara, T. Endo, Chapman-Jouguet oblique detonation structure around hypersonic projectiles, AIAA J. 39 (8) (2001) 1553-1561.

[11] J. Kasahara, T. Arai, S. Chiba, K. Takazawa, Y. Tanahashi, A. Matsuo, Criticality for stabilized oblique detonation waves around spherical bodies in acetylene/oxygen/krypton mixtures, Proc. Combust. Inst. 29 (2) (2002) 2817-2824.

[12] A. Higgins, A. Bruckner, Experimental investigation of detonation initiation by hypervelocity blunt projectiles, AIAA-96-0342, 1996.

[13] J. Verreault, A.J. Higgins, Initiation of detonation by conical projectiles, Proc. Combust. Inst. 33 (2) (2011) 2311-2318.

[14] C. Viguier, L.F. Figueira da Silva, D. Desbordes, B. Deshaies, Onset of oblique detonation waves: comparison between experimental and numerical results for hydrogen-air mixtures, in: twenty-sixth Symposium (International) on Combustion, 26 (2) (1996) 3023-3031.

[15] C.I. Morris, M.R. Kamel, R.K. Hanson, Shock-induced combustion in high-speed wedge flows, in: twenty-seventh Symposium (International) on Combustion, 27 (2) (1998) 2157-2164.

[16] L.F. Figueira da Silva, B. Deshaies, Stabilization of an oblique detonation wave by a wedge: a parametric numerical study, Combust. Flame 121 (1) (2000) 152-166.

[17] M.V. Papalexandris, A numerical study of wedge-induced detonations, Combust. Flame 120 (4) (2000) 526-538.

[18] Y. Liu, D. Wu, S. Yao, J. Wang, Analytical and numerical investigations of wedge-induced oblique detonation waves at low inflow Mach number, Combust. Sci. Technol. 187 (6) (2015) 843-856.

[19] P. Yang, H. Teng, Z. Jiang, H.D. Ng, Effects of inflow Mach number on oblique detonation initiation with a two-step induction-reaction kinetic model, Combust. Flame 193 (2018) 246-256.

[20] J.Y. Choi, D.W. Kim, I.S. Jeung, F. Ma, V. Yang, Cell-like structure of unstable oblique detonation wave from high-resolution numerical simulation, Proc. Combust. Inst. 31 (2) (2007) 2473-2480.

[21] J. Verreault, A.J. Higgins, R.A. Stowe, Formation of transverse waves in oblique detonations, Proc. Combust. Inst. 34 (2) (2013) 1913-1920.

[22] Y. Zhang, L. Zhou, J. Gong, H.D. Ng, H. Teng, Effects of activation energy on the instability of oblique detonation surfaces with a one-step chemistry model, Phys. Fluids 30 (2018) 106110.

[23] Z. Ren, B. Wang, G. Xiang, L. Zheng, Effect of the multiphase composition in a premixed fuel-air

stream on wedge-induced oblique detonation stabilisation, J. Fluid Mech. 846 (2018) 411-427.

[24] Z. Ren, B. Wang, G. Xiang, L. Zheng, Numerical analysis of wedge-induced oblique detonations in two-phase kerosene-air mixtures, Proc. Combust. Inst. 37 (3) (2019) 3627-3635.

[25] Y. Liu, X. Han, S. Yao, J. Wang, A numerical investigation of the prompt oblique detonation wave sustained by a finite-length wedge, Shock Waves 26 (6) (2016) 729-739.

[26] J.Y. Choi, E.J.R. Shin, I.S. Jeung, Unsteady combustion induced by oblique shock waves at the non-attaching condition of the oblique detonation wave, Proc. Combust. Inst. 32 (2) (2009) 2387-2396.

[27] Y. Fang, Z. Hu, H. Teng, Numerical investigation of oblique detonations induced by a finite wedge in a stoichiometric hydrogen-air mixture, Fuel 234 (2018) 502-507.

[28] S. Bhattrai, H. Tang, Formation of near-Chapman-Jouguet oblique detonation wave over a dual-angle ramp, Aerosp. Sci. Technol. 63 (2017) 1-8.

[29] K. Iwata, S. Nakaya, M. Tsue, Wedge-stabilized oblique detonation in an inhomogeneous hydrogen-air mixture, Proc. Combust. Inst. 36 (2) (2017) 2761-2769.

[30] Y. Fang, Z. Hu, H. Teng, Z. Jiang, H.D. Ng, Numerical study of inflow equivalence ratio inhomogeneity on oblique detonation formation in hydrogen-air mixtures, Aerosp. Sci. Technol. 71 (2017) 256-263.

[31] P. Yang, H.D. Ng, H. Teng, Numerical study of wedge-induced oblique detonations in unsteady flow, J. Fluid Mech. 876 (2019) 264-287.

[32] X. Cai, J. Liang, Z. Lin, R. Deiterding, Y. Liu, Parametric study of detonation initiation using a hot jet in supersonic combustible mixtures, Aerosp. Sci. Technol. 39 (2014) 442-455.

[33] X. Cai, J. Liang, R. Deiterding, Z. Lin, Adaptive simulations of cavity-based detonation in supersonic hydrogen-oxygen mixture, Int. J. Hydrogen Energ. 41 (2016) 6917-6928.

[34] X. Cai, J. Liang, R. Deiterding, Numerical investigation on detonation control using a pulse hot jet in

supersonic combustible mixture, Combust. Sci. Technol. 188 (10) (2016) 1674-1690.

[35] J.D. Sterling, E.B. Cummings, K. Ghorbanian, D.T. Pratt, T.H. Sobota, N.J. Brock, M.S. Brown, J. Segall, P.A. DeBarber, Oblique detonation wave studies in the Caltech T-5 Shock tunnel facility, AIAA Paper AIAA-98-1561, 1998.

[36] Z. Lin, J. Zhang, J. Zhou, Design of high-enthalpy premixed supersonic heater and experimental study of oblique detonation, AIAA Paper, 2007-5009, 2007.

[37] R.G. Veraar, A.E.H.J. Mayer, J. Verreault, R.A. Stowe, R. Farinaccio, P.G. Harris, Proof-of-principle experiment of a shock-induced combustion ramjet, AIAA Paper, 2009-7432, 2009.

[38] X. Cai, R. Deiterding, J. Liang, Y. Mahmoudi, Adaptive simulations of viscous detonations initiated by a hot jet using a high-order hybrid WENO-CD scheme, Proc. Combust. Inst. 36 (2017) 2725-2733.

[39] X. Cai, R. Deiterding, J. Liang, M. Sun, Y. Mahmoudi, Diffusion and mixing effects in hot jet initiation and propagation of hydrogen detonations, J. Fluid Mech. 836 (2018) 324-351.

[40] F.K. Lu, H.Y. Fan, D.R. Wilson, Detonation waves induced by a confined wedge, Aerosp. Sci. Technol. 10 (2006) 679-685.

[41] H.Y. Han, F.K. Lu, Numerical modelling of oblique shock and detonation waves induced in a wedged channel, Proc. Inst. Mech. Eng., G J. Aerosp. Eng. 222 (2008) 687-703.

[42] X. Cai, J. Liang, R. Deiterding, Y. Mahmoudi, M. Sun, Experimental and numerical investigations on propagating modes of detonations: Detonation wave/boundary layer interaction, Combust. Flame 190 (2018) 201-215.

[43] C.L. Dailey, Supersonic diffuser instability, PhD thesis, California Institute of Technology, 1954.

[44] S. Trapier, P. Duveau, S. Deck, Experimental study of supersonic inlet buzz, AIAA J. 44 (10) (2006) 2354-2365.

[45] S. Trapier, S. Deck, P. Duveau, Delayed detached-eddy simulation and analysis of supersonic inlet buzz, AIAA J. 46 (1) (2008) 118-131.

[46] W. Gao, Z. Li, J. Yang, Y. Zeng, Effects of trips on the oscillatory flow of an axisymmetric hypersonic inlet with downstream throttle, Chinese J. Aeronaut. 31 (2) (2018) 225-236.

[47] D.T. Pratt, J.W. Humphrey, D.E. Glenn, Morphology of standing oblique detonation waves, J. Propuls. Power 7 (5) (1991) 837-845.

[48] D.C. Alexander, J.P. Sislian, Computational study of the propulsive characteristics of a shcramjet engine, J. Propuls. Power 24 (1) (2008) 34-44.

[49] Y.W. Wang, J.P. Sislian, Numerical simulation of gaseous hydrocarbon fuel injection in a hypersonic inlet, J. Propuls. Power 26 (5) (2010) 1114-1124.

[50] M.K. Smart, N.E. Hass, Flight data analysis of the HyShot 2 scramjet flight experiment, AIAA J. 44 (10) (2006) 2366-2375.

[51] S.J. Laurence, D. Lieber, J.M. Schramm, K. Hannemann, J. Larsson, Incipient thermal choking and stable shock-train formation in the heat-release region of a scramjet combustor. Part I: Shock-tunnel experiments, Combust. Flame 162 (2015) 921-931.

[52] J. Larsson, S. Laurence, I. Bermejo-Moreno, J. Bodart, S. Karl, R. Vicquelin, Incipient thermal choking and stable shock-train formation in the heat-release region of a scramjet combustor. Part II: Large eddy simulations, Combust. Flame 162 (2015) 907-920.

[53] J.P. Sislian, B. Parent, Hypervelocity fuel/air mixing in a shcramjet inlet, J. Propuls. Power 20 (2) (2004) 263-272.

[54] T.E. Schwartzentruber, J.P. Sislian, Suppression of premature ignition in the premixed inlet flow of a shcramjet, J. Propuls. Power 21 (1) (2005) 87-94.

[55] F.R. Menter, Two-equation eddy-viscosity turbulence models for engineering applications, AIAA J. 32 (8) (1994) 1598-1605.

[56] B.J. McBride, S. Gordon, M.A. Reno, Coefficients for calculating thermodynamic and transport properties of individual species, NASA TM-4513, 1993.

[57] C.R. Wilke, A viscosity equation for gas mixtures, J. Chem. Phys. 18 (1950) 517-519.

[58] C.J. Jachimowski, An analytical study of the hydrogen-air reaction mechanism with application to scramjet combustion, NASA TP-2791, 1988.

[59] K. Wu, Investigation on the flame stabilization modes and chemical mechanism reduction in supersonic combustion, PhD thesis, University of Chinese Academy of Sciences, 2018.

[60] J.Y. Choi, Computational fluid dynamics algorithms for unsteady shock-induced combustion, Part 1: Validation, AIAA J. 38 (7) (2000) 1179-1187.

[61] M.P. Burke, M. Chaos, Y. Ju, F.L. Dryer, S.J. Klippenstein, Comprehensive H_2/O_2 kinetic model for high pressure combustion, Int. J. Chem. Kinet. 44 (2011) 444-474.

[62] L. Shi, H. Shen, P. Zhang, D. Zhang, C. Wen, Assessment of vibrational non-equilibrium effect on detonation cell size, Combust. Sci. Technol. 189 (5) (2017) 841-853.

[63] K.C. Uy, L. Shi, C. Wen, Chemical reaction mechanism related vibrational nonequilibrium effect on the Zel'dovich−von Neumann−Döring (ZND) detonation model, Combust. Flame 196 (2018) 174-181.

[64] K.C. Uy, L.S. Shi, C.Y. Wen, Prediction of half reaction length for H_2−O_2−Ar detonation with an extended vibrational nonequilibrium Zel'dovich−von Neumann−Döring (ZND) model, Int. J. Hydrogen Energ. 44 (2019) 7667-7674.

[65] L. Shi, K.C.K Uy, C.Y. Wen, The re-initiation mechanism of detonation diffraction in a weakly unstable gaseous mixture, J. Fluid Mech. 895 (2020) A24.

[66] C. Park, Assessment of two-temperature kinetic model for ionizing air, J. Thermophys. Heat Trans. 3 (3) (1989) 233-244.

[67] S. Chakravarthy, A unified-grid finite volume formulation for computational fluid dynamics, Int. J. Numer. Meth. Fluids 31 (1) (1999) 309-323.

[68] E.F. Toro, Riemann solvers and numerical methods for fluid dynamics: a practical introduction, Springer Science & Business Media, 2013.

[69] D.L. Ropp, J.N. Shadid, Stability of operator splitting methods for systems with indefinite operators: advection-diffusion-reaction systems, J. Comput. Phys. 228 (2009) 3508-3516.

[70] E. Schülein, Skin-friction and heat flux measurements in shock/boundary-layer interaction flows, AIAA J. 44 (8) (2006) 1732-1741.

[71] H.F. Lehr, Experiment on shock-induced combustion, Astronaut. Acta 14 (4-5) (1972) 589-597.

[72] T. Wang, Y. Zhang, H. Teng, Z. Jiang, Numerical study of oblique detonation wave initiation in a stoichiometric hydrogen-air mixture, Phys. Fluids 27 (2015) 096101.

[73] D.W. Riggins, C.R. McClinton, R.C. Rogers, R.D. Bittner, Investigation of scramjet injection strategies for high Mach number flows, J. Propuls. Power 11 (3) (1995) 409-418.

[74] D.W. Riggins, C.R. McClinton, P.H. Vitt, Thrust losses in hypersonic engines part 1: methodology, J. Propuls. Power 13 (2) (1997) 281-287.

[75] J.P. Sislian, R.P. Martens, T.E. Schwartzentruber, Numerical simulation of a real shcramjet flowfield, J. Propuls. Power 22 (5) (2006) 1039-1048.

[76] J. Chan, J.P. Sislian, Numerically simulated comparative performance of a scramjet and shcramjet at Mach 11, J. Propuls. Power 26 (5) (2010) 1125-1134.

[77] Z. Zhang, Oblique detonation propulsion theory, technology and its experimental demonstration, PhD

thesis, University of Chinese Academy of Sciences, 2020.

[78] Z. Jiang, H. Yu, Theories and technologies for duplicating hypersonic flight conditions for ground testing, Natl. Sci. Rev. 4 (3) (2017) 290-296.

Figures

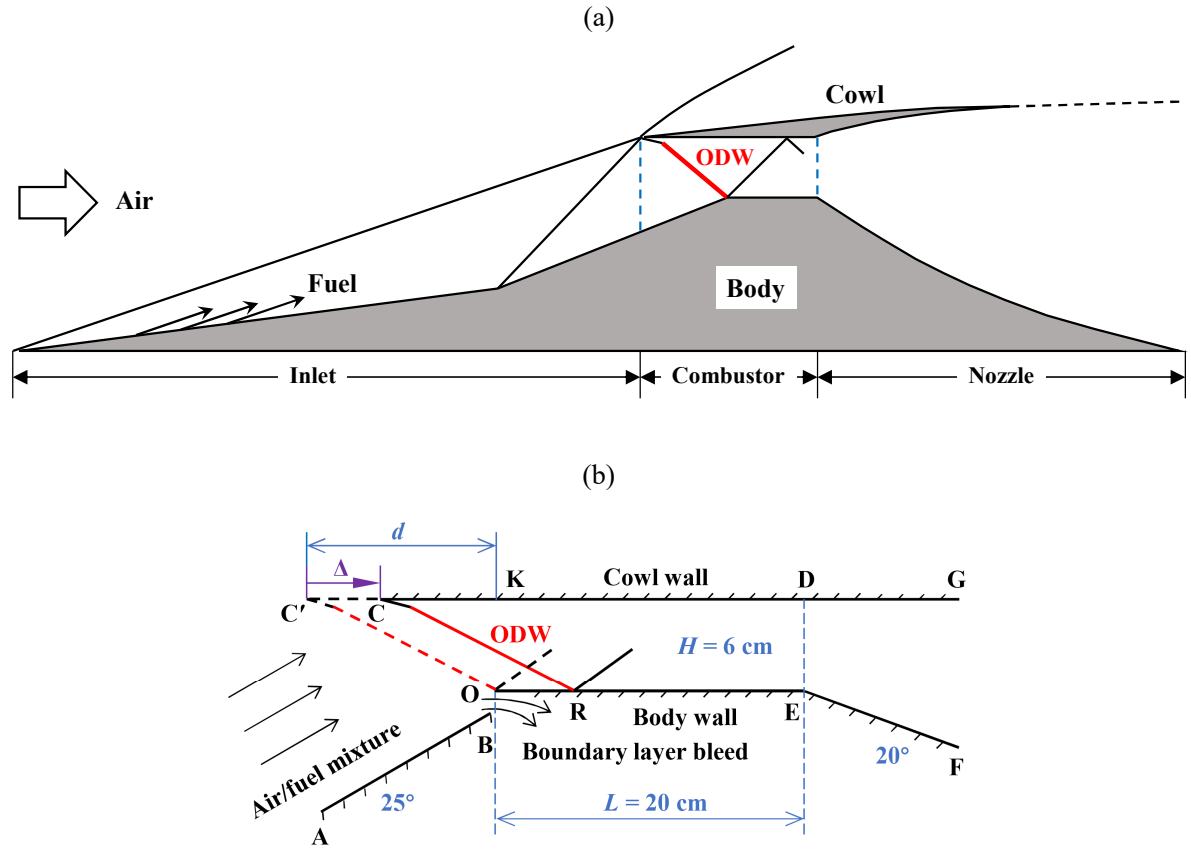

Fig. 1 Schematics of (a) a 2D ODE with a two-ramp inlet and (b) the specific geometry of its combustor.

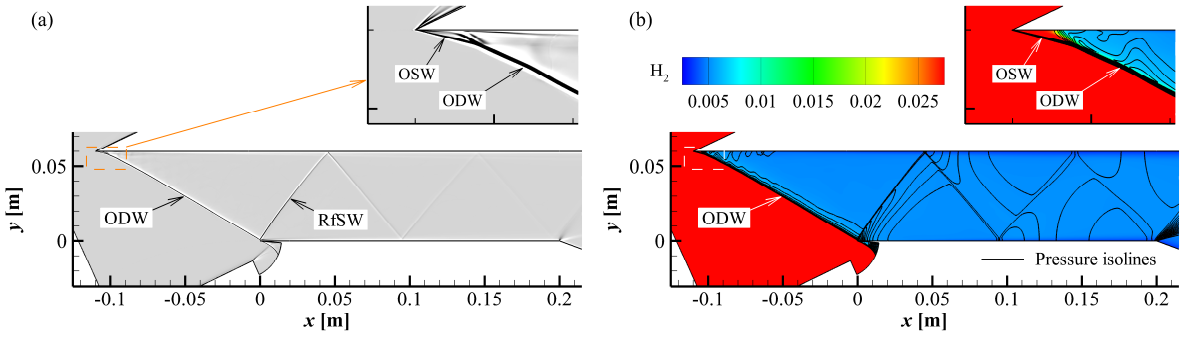

Fig. 2 Flow field in the ODE combustor (Case 1: $\xi = 0$). (a) Shadowgraph and (b) contour of H_2 mass

fraction.

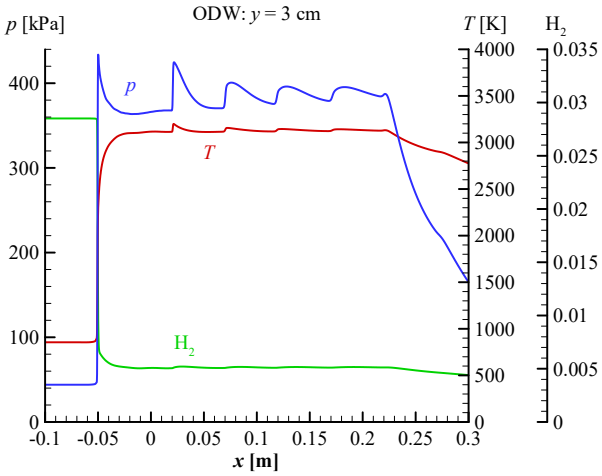

Fig. 3 Flow parameters along the centerline of the ODE combustor (y = 3 cm, Case 1: ξ = 0).

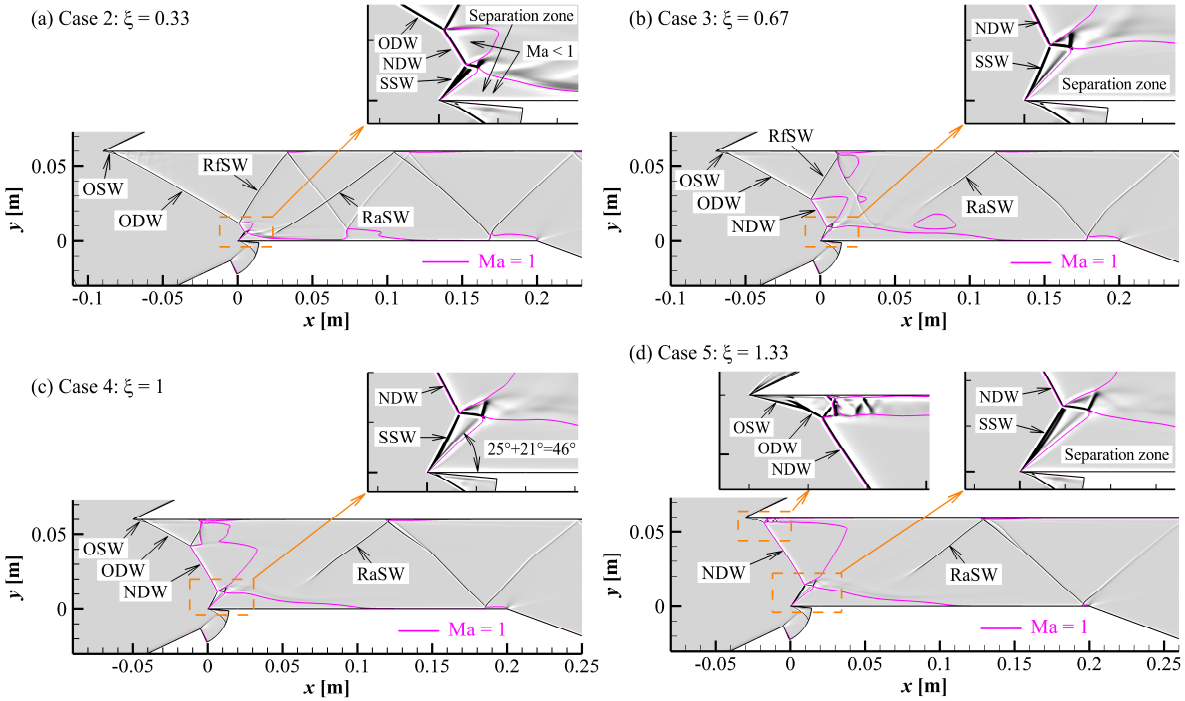

Fig. 4 Numerical shadowgraphs of the flow fields in ODE combustors with different geometries (ξ).

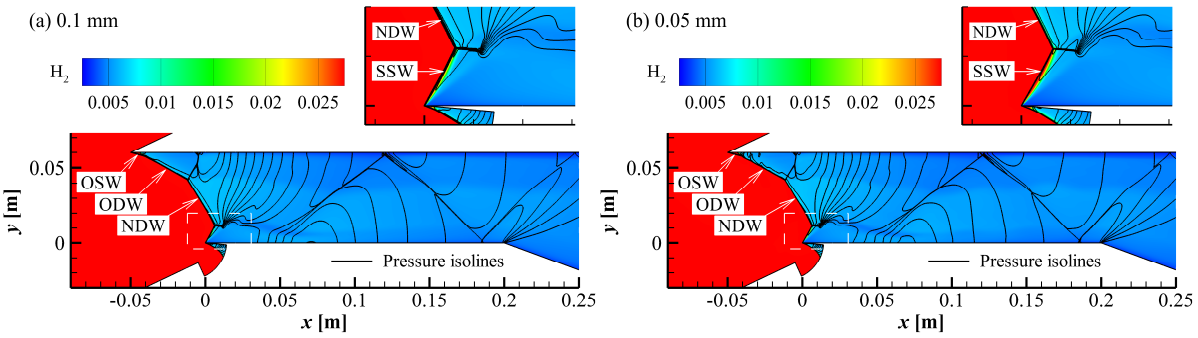

Fig. 5 Contours of H_2 mass fraction in the ODE combustor with different grid sizes (Case 4: $\xi = 1$).

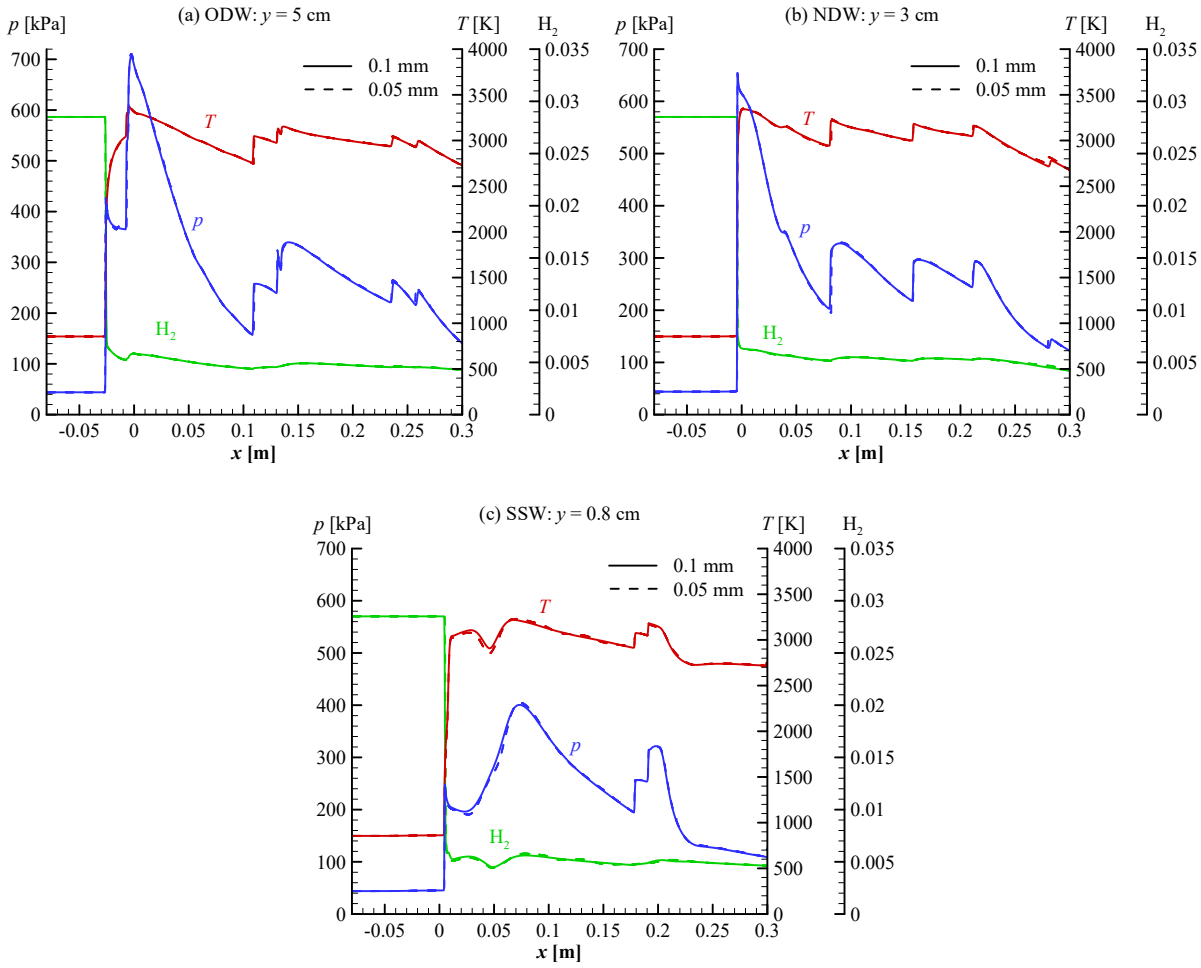

Fig. 6 Pressure, temperature, and H_2 distributions at (a) $y = 5$ cm, (b) $y = 3$ cm and (c) $y = 0.8$ cm in the ODE combustor (Case 4: $\xi = 1$).

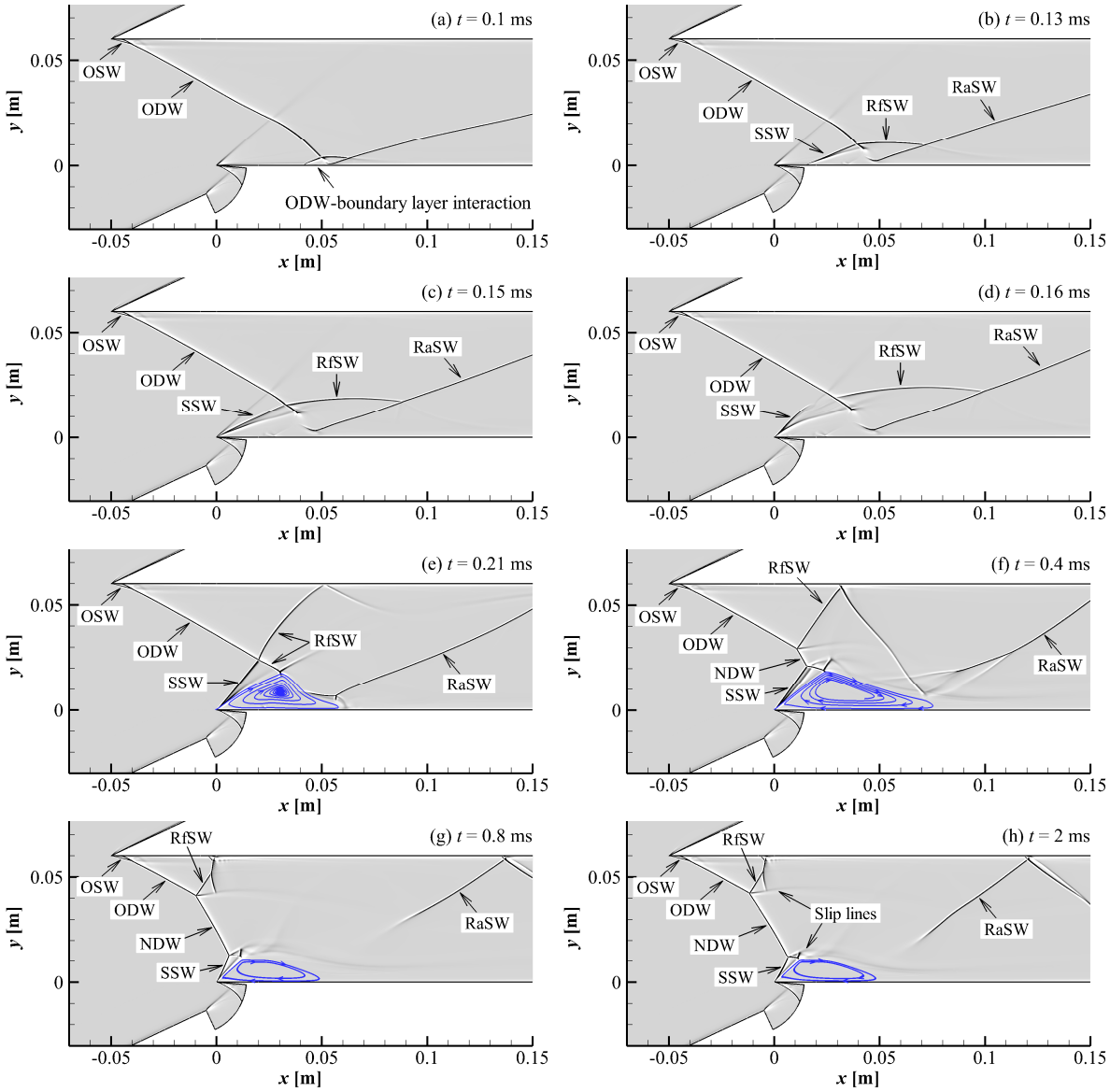

Fig. 7 Establishment of the flow field in the ODE combustor (Case 4: $\xi = 1$).

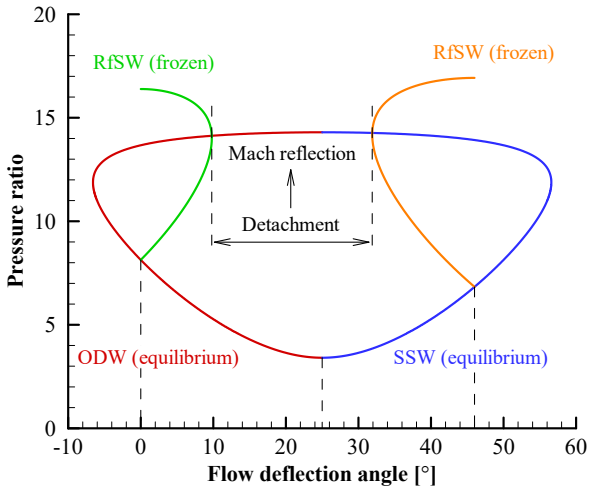

Fig. 8 Shock polar analysis of oblique detonation reflection (Case 4: $\xi = 1$).

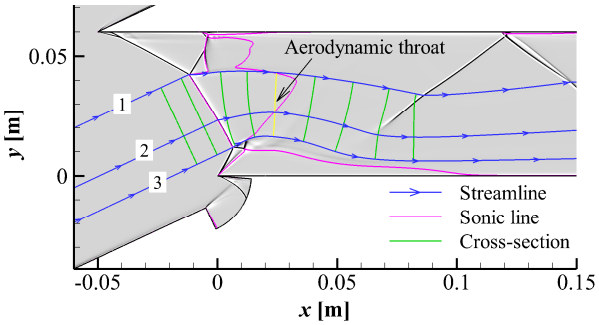

Fig. 9 The effective aerodynamic convergent-divergent nozzle (bounded by Streamlines 1 and 2) formed in the ODE combustor (Case 4: $\xi = 1$).

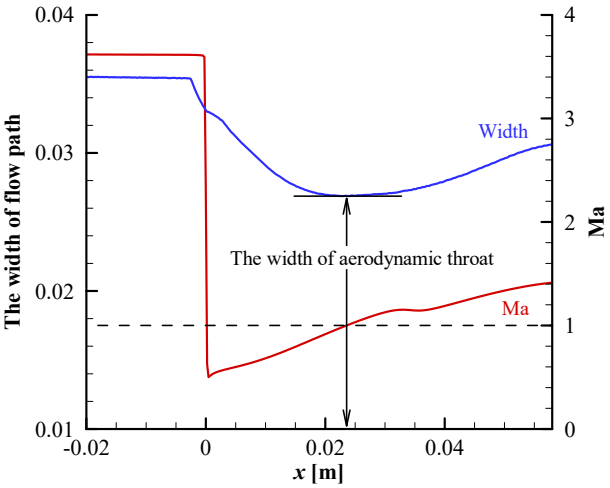

Fig. 10 The width of the flow path in the effective aerodynamic nozzle and the distribution of Mach number along Streamline 2 (from Fig. 9; Case 4: $\xi = 1$).

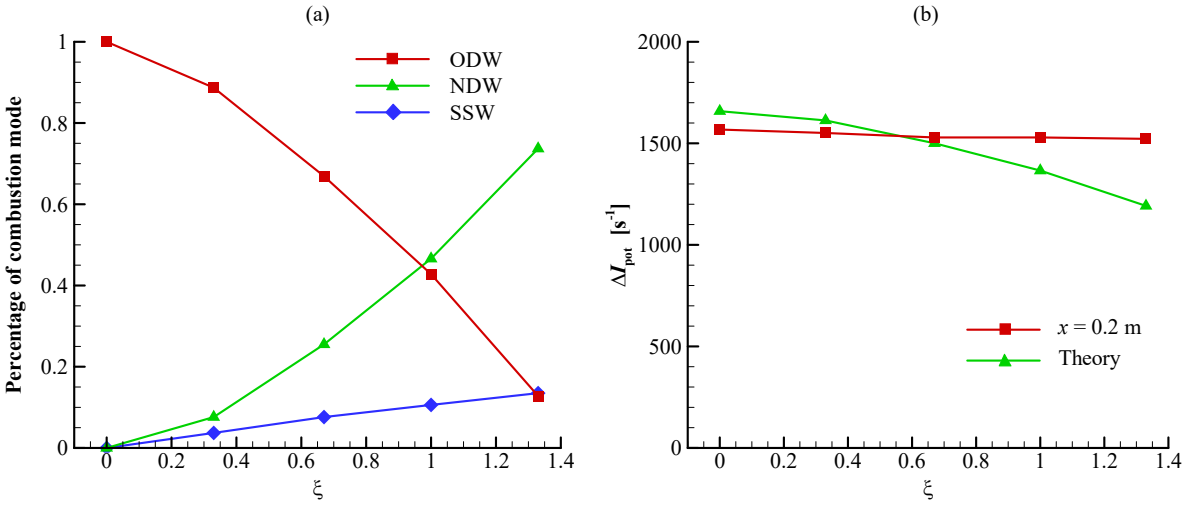

Fig. 11 Thrust performance of ODE combustors with different geometries. (a) Percentages of different combustion modes and (b) total thrust potential additions at combustor outlet (x = 0.2 m).

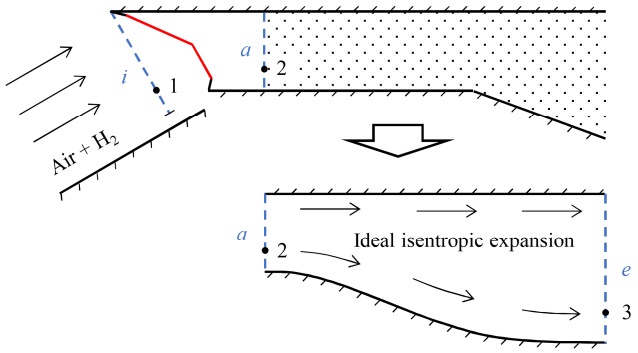

Fig. 12 Ideal isentropic expansion for estimating thrust potential at an arbitrary plane a.

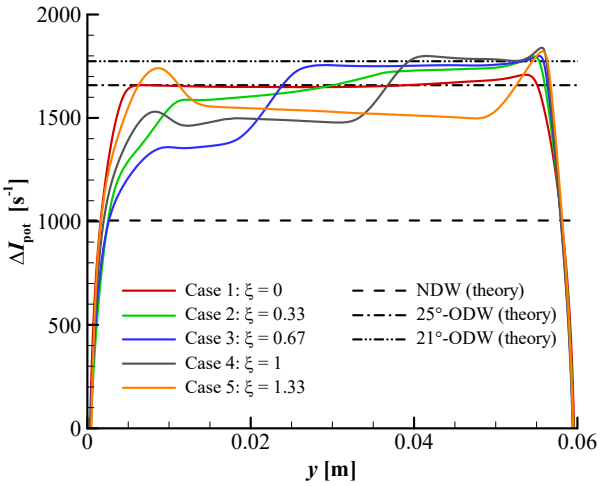

Fig. 13 Thrust potential addition along the combustor's height at the outlet (x = 0.2 m).

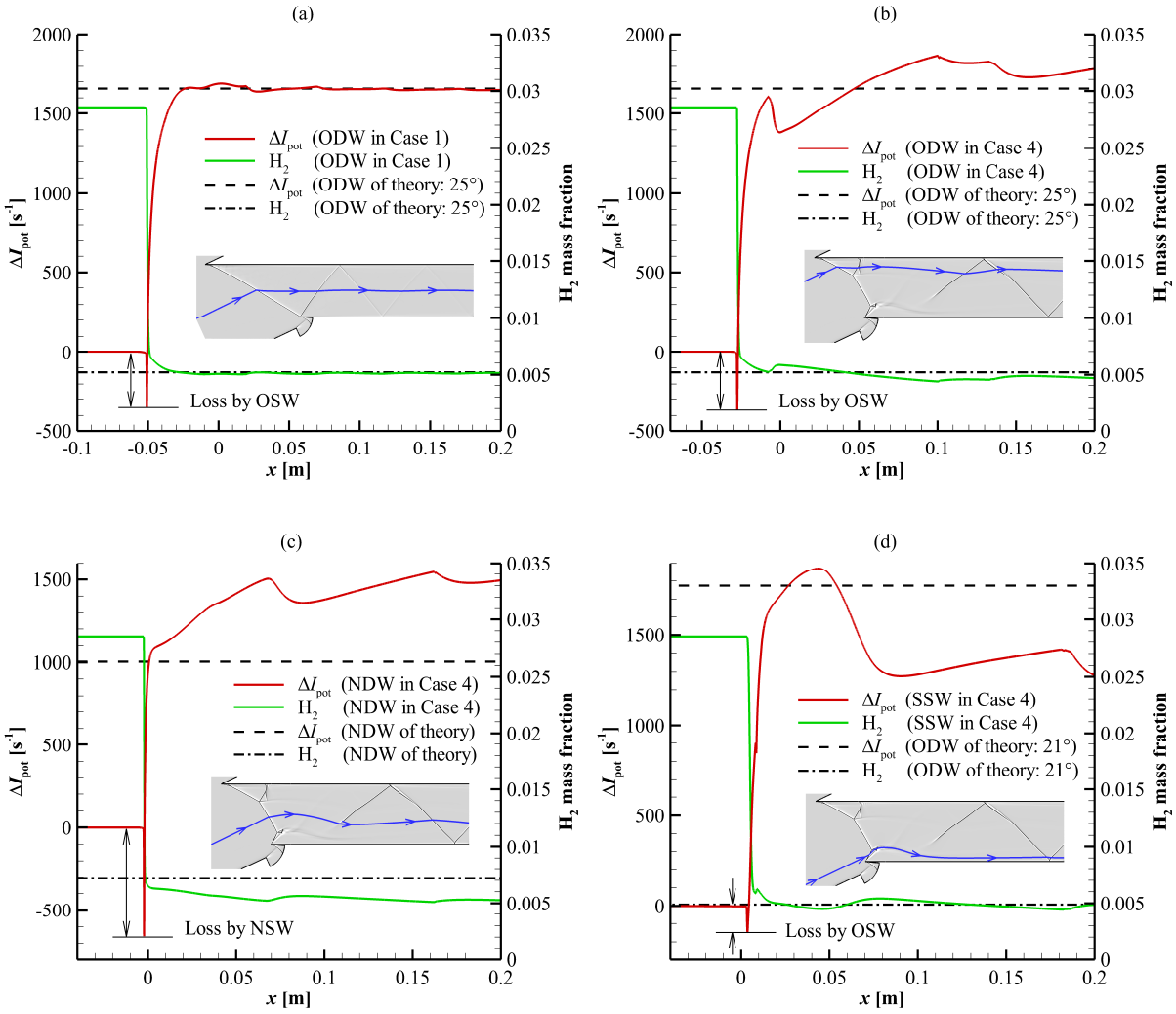

Fig. 14 Thrust potential additions along the streamlines across (a) ODW in Case 1, (b) ODW in Case 4, (c)

NDW in Case 4 and (d) SSW in Case 4.